nature communications

Article

https://doi.org/10.1038/s41467-024-48122-6

Facilitating the dry reforming of methane with interfacial synergistic catalysis in an $Ir@CeO_{2-x}$ catalyst

Received: 17 October 2023

Accepted: 19 April 2024

Published online: 04 May 2024

Check for updates

Hui Wang[1], Guoqing Cui[2] ✉, Hao Lu[1], Zeyang Li[1], Lei Wang[1,3], Hao Meng[1,3], Jiong Li[4], Hong Yan[1], Yusen Yang[1,3] ✉ & Min Wei[1,3] ✉

The dry reforming of methane provides an attractive route to convert greenhouse gases (CH_4 and CO_2) into valuable syngas, so as to resolve the carbon cycle and environmental issues. However, the development of high-performance catalysts remains a huge challenge. Herein, we report a 0.6% Ir/CeO_{2-x} catalyst with a metal-support interface structure which exhibits high CH_4 (~72%) and CO_2 (~82%) conversion and a CH_4 reaction rate of ~973 μmol_{CH4} g_{cat}^{-1} s^{-1} which is stable over 100 h at 700 °C. The performance of the catalyst is close to the state-of-the-art in this area of research. A combination of in situ spectroscopic characterization and theoretical calculations highlight the importance of the interfacial structure as an intrinsic active center to facilitate the CH_4 dissociation (the rate-determining step) and the CH_2* oxidation to CH_2O* without coke formation, which accounts for the long-term stability. The catalyst in this work has a potential application prospect in the field of high-value utilization of carbon resources.

Owing to the increasing global warming and climate change issues, strategies for greenhouse gas reduction have drawn extensive interest from both fundamental research and industrial applications[1–3]. CO_2 and CH_4 are regarded as two predominant contributors to the greenhouse effect; therefore, their utilization and conversion to high-value-added chemicals and fuels meet the demands for achieving large-scale carbon fixation, carbon emission reduction and carbon cycle[4–7]. One promising approach is to convert both CO_2 and CH_4 simultaneously through thermo-catalytic dry reforming of methane (DRM) reaction, which produces the syngas (H_2 and CO) as an important platform for alternatives of petroleum-derived fuels and valuable chemicals[8–11]. Thermodynamically, the DRM reaction involves both C–H bond dissociation (439 kJ mol^{-1}) and C=O bond hydrogenation (750 kJ mol^{-1}) followed by subsequent formation of CO and H_2, resulting in a highly endothermic process (ΔH_{298K} = 247 kJ mol^{-1})[12–15]. This normally requires a high energy consumption and rigorous reaction temperature (>800 °C) to maintain favorable catalytic activity, but suffers from serious catalyst deactivation due to nanoparticle agglomeration and carbon deposition[16–18]. In this case, great efforts have been focused on the exploration of catalysts towards DRM reaction, such as supported noble metals (e.g., Pt[19], Ru[9,20], and Pd[21,22]) and non-noble metals (e.g., Ni[23–25] and Co[26]) catalysts. Although considerable advances have been made, rational design and preparation of highly efficient catalysts to acquire high activity and stability simultaneously, still remain a big challenge.

In general, pure metal surfaces exhibit low reactivity towards methane dissociation and are prone to deactivation resulting from carbon deposition; whilst both experimental and theoretical studies have shown that C–H bond activation is more sensitive to coordinatively unsaturated metallic sites[12,27]. In this respect, the emerging strong metal-support interaction (SMSI) has demonstrated many appealing advantages, such as the interfacial structure and synergistic

[1]State Key Laboratory of Chemical Resource Engineering, Beijing Advanced Innovation Center for Soft Matter Science and Engineering, Beijing University of Chemical Technology, 100029 Beijing, P. R. China. [2]State Key Laboratory of Heavy Oil Processing, China University of Petroleum (Beijing), 102249 Beijing, P. R. China. [3]Quzhou Institute for Innovation in Resource Chemical Engineering, 324000 Quzhou, P. R. China. [4]Shanghai Synchrotron Radiation Facility, Shanghai Institute of Applied Physics, Chinese Academy of Sciences, 201204 Shanghai, P. R. China. ✉e-mail: cui@cup.edu.cn; yangyusen@buct.edu.cn; weimin@mail.buct.edu.cn

catalysis, which have attached widespread research interest in various heterogeneous reactions (e.g., CO_2 methanation and water gas shift reaction)[28–31]. The fine-tuning for SMSI has been successfully employed to optimize geometric/electronic structure of metal species at the interface[32–34], which provides great opportunities to promote catalytic performance towards DRM reaction. On the one hand, the oxidic $M^{\delta+}$ metal species formed at the interfacial sites as an electron−acceptor, would reduce the T_d symmetry structure of methane molecule and thus facilitate its activation dehydrogenation to CH_x[6,12,20]. For instance, Pirovano et al. reported that Ni^{2+} species promotes C−H bond dissociation at a lower temperature relative to metal Ni based on experiments and DFT calculations[35]. On the other hand, reducible supports (e.g., CeO_2, ZrO_2, and TiO_2), which renders a facile conversion between two oxidation states (e.g., Ce^{4+} and Ce^{3+}), would stabilize oxidic $M^{\delta+}$ species via accommodating metal-to-support electron transfer[32,36–38]. Meanwhile, the concomitant oxygen vacancies make a great contribution to elevate the activation adsorption of C=O group and facilitate the transformation of intermediates[34,39,40]. For example, Liu et al. reported the oxygen vacancies on CeO_2 surface serve as active center towards CO_2 hydrogenation to methanol, where the catalytic activity is highly correlated with the oxygen vacancies concentration[41]. This evokes us to design a suitable metal-support interface structure with synergistic catalysis effect, so as to simultaneously promote catalytic activity and stability for DRM reaction and further reveal the structure-property correlation at molecular/atomic scale.

Herein, we report an Ir nanoclusters supported on CeO_2 catalyst prepared through a facile impregnation-reduction method. HAADF-STEM, *quasi* in situ XPS and in situ XAFS confirm the formation of interface structure ($Ir^{\delta+}$–O_v–Ce^{3+}), whose concentration can be modulated via adjusting the Ir loading. The optimal catalyst 0.6% Ir/CeO_{2-x} (Fig. 1a) exhibits high conversions of CH_4 (~72%) and CO_2 (~82%) at 700 °C, with a CH_4 reaction rate of ~973 $\mu mol_{CH4}\ g_{cat}^{-1}\ s^{-1}$; and a 100 h stream-on-line test demonstrates a satisfactory stability without obvious deactivation. This is, to the best of our knowledge, preponderant to the state-of-the-art catalysts under similar reaction conditions. Kinetics studies verify that the dissociation of CH_4 is the rate-determining step in DRM reaction, whose activation energy decreases significantly by ~50 kJ mol^{-1} owing to the interfacial

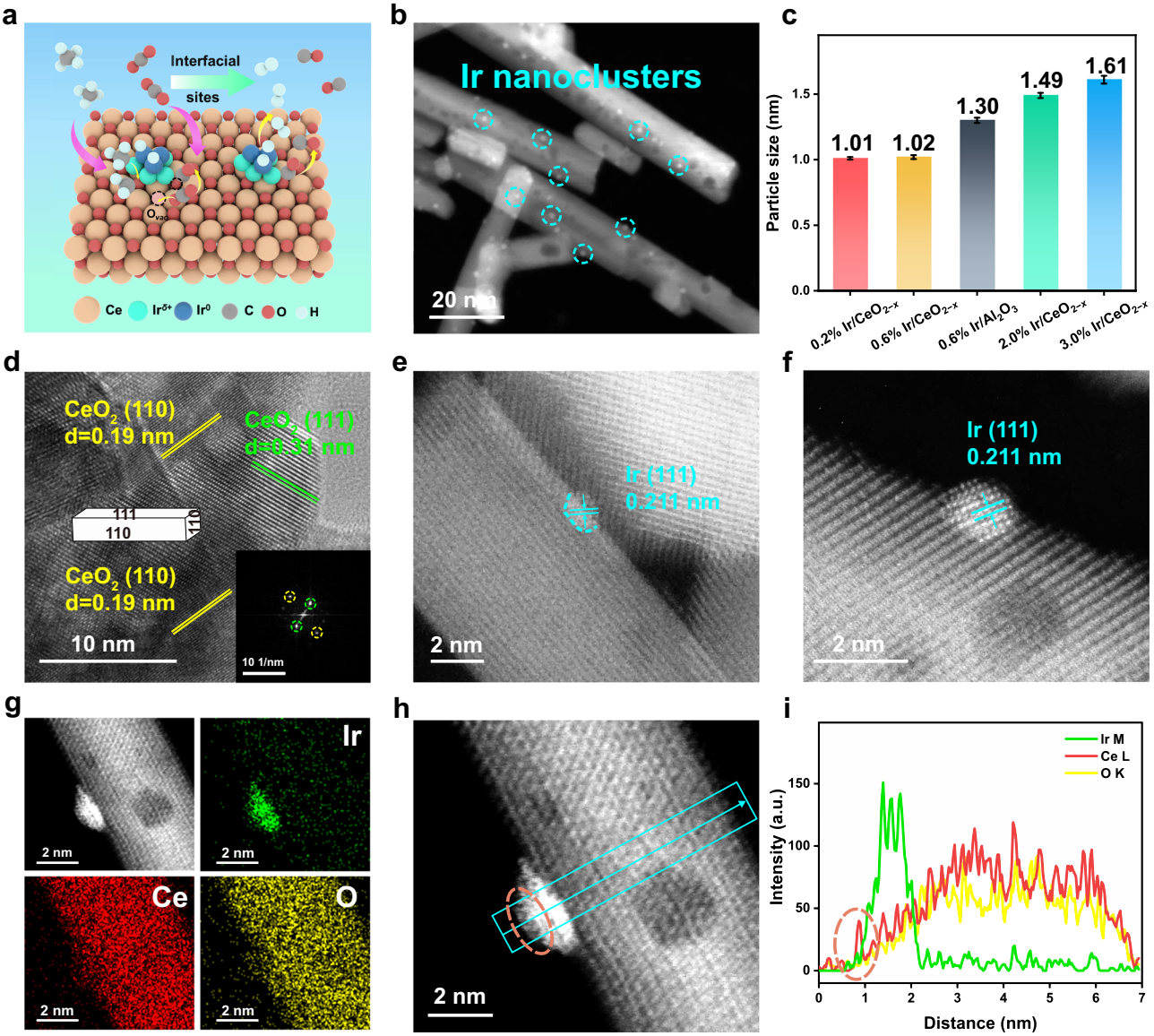

Fig. 1 | Microstructure and morphology studies of Ir/CeO_{2-x} samples. **a** Schematic illustration of Ir/CeO_{2-x} samples. **b**, **d** TEM and HR-TEM images of 0.6% Ir/CeO_{2-x}. **c** Particle size of various Ir/CeO_{2-x} and Ir/Al_2O_3 samples determined by TEM. **e**, **f** High-resolution AC-HAADF-STEM images of 0.2% and 0.6% Ir/CeO_{2-x}, respectively. **g**, **h** AC-HAADF-STEM image and corresponding EDS mapping of 0.6% Ir/CeO_{2-x}. **i** Corresponding elemental line scanning of 0.6% Ir/CeO_{2-x}.

https://doi.org/10.1038/s41467-024-48122-6

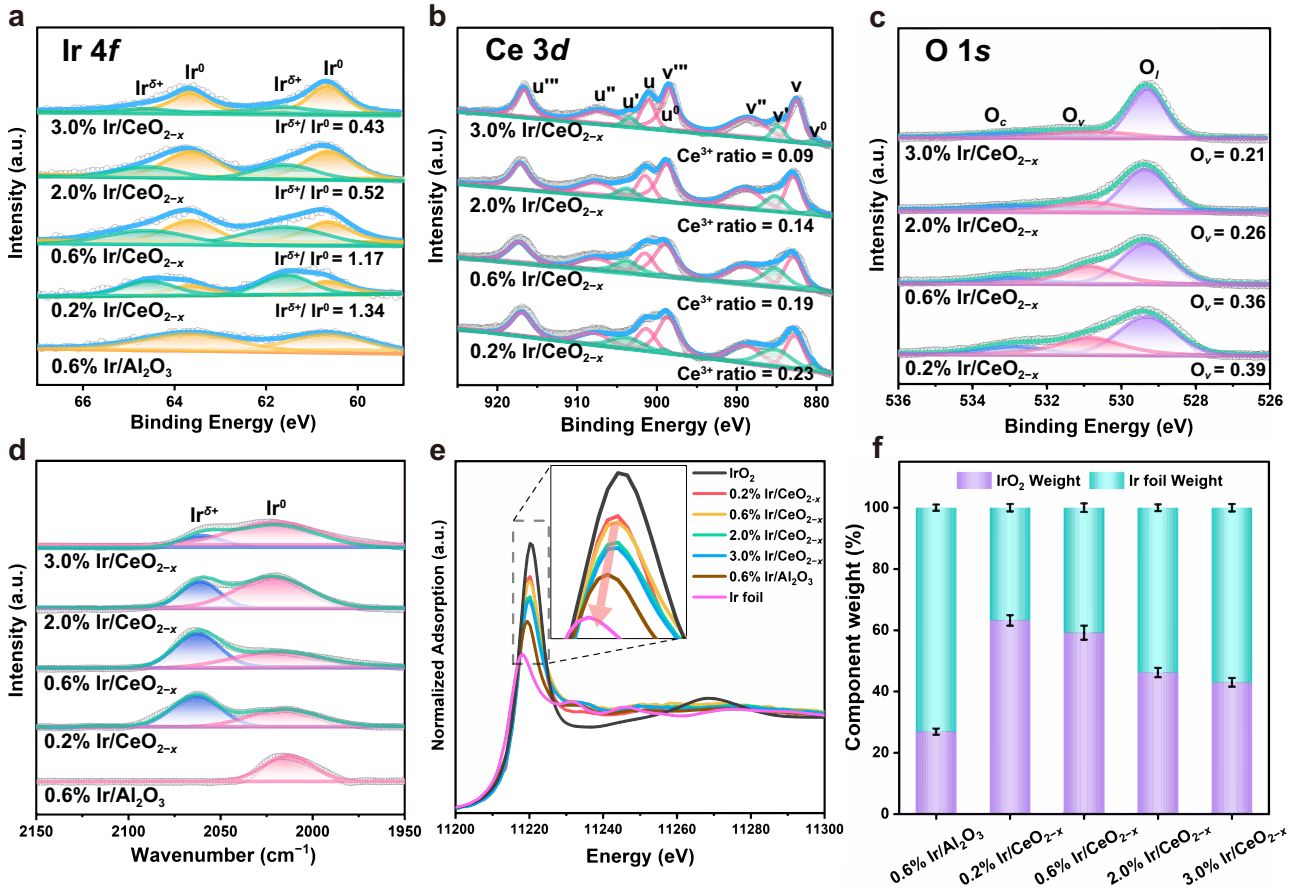

Fig. 2 | Fine-structure characterizations of Ir/Al_2O_3 and Ir/CeO_{2-x} samples. **a**–**c** *Quasi* in situ XPS of Ir 4*f*, Ce 3*d* an O 1*s* for Ir/Al_2O_3 and Ir/CeO_{2-x} samples with various Ir loading. **d** In situ CO-DRIFTS spectra on the surface over Ir/Al_2O_3 and various Ir/CeO_{2-x} samples. **e** Ir L_3-edge XANES spectra and (**f**) diagram of the linear combination fitting (LCF) results for various samples.

synergistic catalysis. *Operando* investigations (DRIFTS and XAFS), catalytic evaluations and DFT calculations substantiate that the interfacial sites ($Ir^{\delta+}$–O_v–Ce^{3+}) serve as the intrinsic active center: CH_4 molecule undergoes activation adsorption and dissociation to CH_2* species and H_2 at the interfacial $Ir^{\delta+}$ site, and then CH_2* experiences oxidation by neighboring oxygen species to generate CH_2O*, followed by CH_2O* dehydrogenation to produce CO and H_2; the concomitant O_v is replenished by the activation adsorption of C=O group in CO_2. This interfacial synergistic catalysis not only enhances the catalytic activity for DRM reaction, but also inhibits catalyst deactivation from excessive decomposition of CH_2* species to carbon deposition.

Results and discussion

Structural characterizations of catalysts

Both Ir/Al_2O_3 and Ir/CeO_{2-x} samples with various Ir loading (0.2%–3%) were prepared via a facile impregnation-reduction method, whose XRD patterns (Supplementary Fig. 1) displayed a series of characteristic reflections indexed to a typical Al_2O_3 (JCPDS 77-0396) and CeO_2 (JCPDS 78-0694) phase, respectively. No recognizable diffractions peaks of Ir or IrO_2 are found for these samples, implying a highly dispersed Ir species and/or a low Ir content. TEM images of Ir/CeO_{2-x} samples (Fig. 1b) show numerous Ir nanoclusters are well dispersed and anchored onto the CeO_2 nanorods support, in which the mean particle size of Ir increases from ~1.0 nm (0.2% and 0.6% Ir/CeO_{2-x}) to ~1.5 nm (2% Ir/CeO_{2-x}) and then to ~1.6 nm (3.0% Ir/CeO_{2-x}) (Fig. 1c and Supplementary Fig. 4–7). Accordingly, the dispersion of Ir (D_{Ir}, Supplementary Table 1) decreases gradually from 82% (0.2% Ir/CeO_{2-x}) to 39% (3.0% Ir/CeO_{2-x}). From the local magnification HR-TEM images (Fig. 1d and Supplementary Fig. 3–7), two clear crystalline phases are identified as ~0.19 and ~0.31 nm, respectively, corresponding to the (110) and (111) planes of CeO_2 nanorods support. As shown in Supplementary Fig. 8, the (110) facet is predominantly exposed accompanied with minor (111) facet, consistent with the previous reports[41,42]. As a control sample, 0.6% Ir/Al_2O_3 displays a larger particle size (~1.3 nm) and a lower dispersion (~65%) relative to 0.6% Ir/CeO_{2-x}, along with lattice spacings of ~0.19 and ~0.23 nm ascribed to (400) and (311) planes of Al_2O_3[43]. In addition, the aberration-correction high-angle annular dark-field scanning transmission electron microscopy (AC-HAADF-STEM) was conducted to explore detailed structure of Ir/CeO_{2-x}. As shown in Fig. 1e and f, a clear lattice fringe (~0.211 nm) indexed to Ir(111) plane is observed on the surface of CeO_2 for both the 0.2% and 0.6% Ir/CeO_{2-x} samples. Moreover, the energy dispersive spectroscopy (EDS) elemental mapping and elemental line scanning of 0.6% Ir/CeO_{2-x} sample (Fig. 1g–i) show a partial coating of CeO_2 on the surface of Ir cluster, indicating the formation of interfacial structure between Ir and CeO_2.

Quasi in situ XPS spectra were performed to investigate the electronic structure of surface Ir species. As shown in Fig. 2a, the Ir/Al_2O_3 sample displays two peaks at 60.6 eV (Ir $4f_{7/2}$) and 63.6 eV (Ir $4f_{5/2}$) corresponding to the Ir^0 species. In contrast, for the four Ir/CeO_{2-x} samples, besides the same Ir^0 peaks, two additional strong peaks at 61.6 eV (Ir $4f_{7/2}$) and 64.6 eV (Ir $4f_{5/2}$) are found, which are attributed to the $Ir^{\delta+}$ species[44–46]. This indicates the electron transfer from Ir species to CeO_2 support at the interface via the electronic metal-support interaction (EMSI), which is absent in the Ir/Al_2O_3 sample. With the increase of Ir content, the ratio of $Ir^{\delta+}/(Ir^{\delta+}+Ir^0)$ declines gradually from 57% (0.2% Ir/CeO_{2-x}) to 30% (3.0% Ir/CeO_{2-x}) (Supplementary Table 2), as a result of the decreased Ir dispersion degree. Furthermore, in situ

CO-DRIFTS is implemented to investigate the configuration of Ir species (Fig. 2d), from which a broad band centered at ~2020 cm^{-1} due to the linear CO at Ir^0 site is found for the Ir/Al_2O_3 sample. Notably, in the case of Ir/CeO_{2-x} samples, both the linear adsorption of CO at Ir^0 (~2020 cm^{-1}) and gem-dicarbonyl species adsorption at $Ir^{\delta+}$ (~2060 cm^{-1}) are observed[44,45,47]. With the increment of Ir loading, according to the Gaussian peak fitting results, the relative peak intensity of $Ir^{\delta+}/(Ir^{\delta+}+Ir^0)$ displays an obvious decrease from 0.2% Ir/CeO_{2-x} (56%) to 3.0% Ir/CeO_{2-x} (23%) (Supplementary Table 3), in accordance with the variation tendency of $Ir^{\delta+}/(Ir^{\delta+}+Ir^0)$ in the XPS results.

X-ray absorption near-edge structure (XANES) measurements at normalized Ir L_3-edge were implemented to analyze the electronic state and coordination fine structure. As shown in Fig. 2e, the white line peaks of Ir/CeO_{2-x} and Ir/Al_2O_3 samples are located between Ir foil and IrO_2 reference, suggesting the existence of positively charged Ir species. Moreover, the intensity of white line declines gradually from 0.2% Ir/CeO_{2-x} to 3.0% Ir/CeO_{2-x} and then to Ir/Al_2O_3, indicating the decrease in the oxidation state of $Ir^{\delta+}$ species (reduced interfacial electron transfer) along with the increase in metallic Ir^0. The Fourier transforms of the extended X-ray absorption fine spectra (EXAFS) in the R space (Supplementary Fig. 10) show that all these samples exhibit coexistent of Ir−O scattering (~1.5 Å) and Ir−Ir scattering (~2.5 Å). Accordingly, we conducted the linear combination fitting (LCF) of XANES (Fig. 2f) to determine the Ir species composition in these samples. The control sample Ir/Al_2O_3 displays a low Ir^{4+} atomic ratio of 27%. In contrast, the Ir^{4+} is predominant for the Ir/CeO_{2-x} samples, in which the Ir^{4+} atomic ratio of 0.2% and 0.6% Ir/CeO_{2-x} samples are 63% and 59% (Supplementary Table 4), respectively; whilst the Ir^0 plays a leading role for the 2.0% and 3.0% Ir/CeO_{2-x} samples, as a result of the increased particle size of Ir. The average oxidation state of iridium species is calculated based on the results from LCF analysis, which gives the following sequence: 0.2% Ir/CeO_{2-x} (+2.5) > 0.6% Ir/CeO_{2-x} (+2.4) > 2.0% Ir/CeO_{2-x} (+1.8) > 3.0% Ir/CeO_{2-x} (+1.7) > 0.6% Ir/Al_2O_3 (+1.1).

Then, we used *quasi* in situ XPS to study the defective sites of Ir/CeO_{2-x} samples, which contribute to mediate the CO_2 activation. For the pristine CeO_2 support (Supplementary Fig. 13), the spectra of Ce 3*d* show six strong peaks at 882.9, 889.0, 898.6 eV (marked as v, v″, and v‴, respectively) and 901.5, 907.6, 917.2 eV (marked as u, u″, and u‴, respectively) assigned to $3d^{10}4f^0$ state of Ce^{4+} species, with a spin-orbit splitting of about 18.6 eV. In terms of Ir/CeO_{2-x} samples (Fig. 2b), four peaks appear at 880.5 eV, 885.2 eV, 899.1 eV, and 903.8 eV (marked as v^0, v′, u^0, and u′, respectively) belonging to $3d^{10}4f^1$ state of Ce^{3+} [41,48]. The relative concentration of surface Ce^{3+}, calculated by $Ce^{3+}/(Ce^{3+}+Ce^{4+})$ based on corresponding peak areas (Supplementary Table 2), decreases gradually from 23% (0.2% Ir/CeO_{2-x}) to 10% (3.0% Ir/CeO_{2-x}). Moreover, the oxygen vacancies of Ir/CeO_{2-x} and Ir/Al_2O_3 samples were further analyzed via deconvolution of *quasi* in situ O 1*s* XPS spectra. As shown in Fig. 2c, three peaks are found at 529.3, 530.8 and above 532.8 eV, which are assigned to the lattice oxygen (O_l), oxygen vacancies (O_v) and other weakly bound oxygen species (O_c, such as hydroxyl oxygen or chemisorbed oxygen species), respectively[48,49]. The relative ratio of oxygen vacancy (O_v) calculated as $O_v/(O_l+O_v+O_c)$ ranks in the following order: 0.2% Ir/CeO_{2-x} (39%) > 0.6% Ir/CeO_{2-x} (36%) > 2.0% Ir/CeO_{2-x} (26%) > 3.0% Ir/CeO_{2-x} (21%) (Supplementary Table 2), in agreement with the tendency of $Ce^{3+}/(Ce^{3+}+Ce^{4+})$ ratio. Therefore, in situ CO-DRIFTS, XAFS and *quasi* in situ XPS results notarize the formation of interface structure ($Ir^{\delta+}$–O_v–Ce^{3+}) originating from SMSI, whose relative concentration decreases with increment of Ir loading.

Catalytic evaluations

The preceding samples were evaluated for DRM under a gas hourly space velocity as high as 240000 mL g^{-1} h^{-1} at atmospheric pressure. As shown in Fig. 3a and b, both the CH_4 and CO_2 conversions as a function of reaction temperature show a positive correlation for these samples, duo to the strong endothermic characteristic. The control sample 0.6% Ir/Al_2O_3 gives a normal catalytic performance towards DRM reaction; whilst the catalytic performance of Ir/CeO_{2-x} samples improve significantly. Notably, the catalytic activity exhibits a volcanic curve at each reaction temperature along with the increase of Ir loading: an increase from 0.2% Ir/CeO_{2-x} to 0.6% Ir/CeO_{2-x} (the maximum value) is present, followed by a slight descend to 2.0% Ir/CeO_{2-x} and 3.0% Ir/CeO_{2-x}. As for the optimal 0.6% Ir/CeO_{2-x} sample, both the CH_4 and CO_2 conversions reach up to the thermodynamic equilibrium, and the reaction rate is 3–20 times higher than previously reported studies under similar reaction conditions within 650–750 °C (Fig. 3c and Supplementary Table 5)[19,50]. Specifically, the 0.6% Ir/CeO_{2-x} catalyst exhibits high conversions of CH_4 (72%) and CO_2 (82%) with a CH_4 reaction rate of ~973 μmol_{CH4} g_{cat}^{-1} s^{-1} at a relatively moderate temperature (700 °C), which are precedent to the state-of-the-art catalysts[6,7,9,16,20,24,25,49–51]. In addition, the long-term stability test displays a rapid deactivation for the Ir/Al_2O_3 sample within 15 h due to Ir agglomeration and carbon deposition at 700 °C (Supplementary Fig. 16 and 17). In contrast, both the CH_4 and CO_2 conversions of 0.6% Ir/CeO_{2-x} catalyst remain almost unchanged within 100 h on stream (Fig. 3d). Moreover, the used 0.6% Ir/CeO_{2-x} catalyst does not show obvious structural change compared with the fresh sample, verified by TEM, XPS and in situ CO-DRIFTS (Supplementary Fig. 18–20), indicating a satisfactory stability in DRM reaction. The results above demonstrate excellent performance of 0.6% Ir/CeO_{2-x} catalyst, which shows potential application in industrial applications.

Furthermore, we performed kinetic studies on CH_4 and CO_2 activation as well as the rate-determining step in DRM system. Firstly, the effects of external and internal diffusion limitation have been eliminated under the aforementioned reaction conditions[34,50,52]. On this basis, the kinetic experimental data were studied via setting a stationary partial pressure of one reactant whilst changing the other partial pressure (Fig. 3e, f), and the obtained results were calculated for kinetic parameters and were shown in Supplementary Table 6. The reaction rate over 0.6% Ir/CeO_{2-x} catalyst displays a linear positive correlation with the partial pressure of CH_4 and CO_2. Nevertheless, the calculated reaction order with respect to CH_4 (~0.67 and ~0.53) is significantly higher than that of CO_2 (~0.09 and ~0.07), indicating that the CH_4 activation is critical to the reaction kinetics, consistent with previous studies[50,52,53]. Moreover, the apparent activation energy (E_a) of CH_4 over 0.6% Ir/CeO_{2-x} is 91 kJ mol^{-1}, much larger than that of CO_2 (70 kJ mol^{-1}) (Fig. 3g and Supplementary Fig. 22 and 23). The results verify that the CH_4 dissociation entails a higher energy barrier and serves as the rate-determining step in this catalytic system. Notably, the E_a value on 0.6% Ir/CeO_{2-x} catalyst shows a marked decline by 35% relative to the 0.6% Ir/Al_2O_3 sample, which indicates the interfacial sites play a critical role in activating reactant molecule. In addition, the intrinsic TOF of CH_4 is evaluated at a low conversion (below 15%, Fig. 3h), which gives a decrease order as follows: 0.2% Ir/CeO_{2-x} (168 mol_{CH4} mol_{Ir}^{-1} s^{-1}) > 0.6% Ir/CeO_{2-x} (163 mol_{CH4} mol_{Ir}^{-1} s^{-1}) > 2.0% Ir/CeO_{2-x} (122 mol_{CH4} mol_{Ir}^{-1} s^{-1}) > 3.0% Ir/CeO_{2-x} (110 mol_{CH4} mol_{Ir}^{-1} s^{-1}). To further the reveal correlation of intrinsic active site and structure-property, the intrinsic TOF of CH_4 is plotted as a function of interfacial $Ir^{\delta+}$ concentration (based on the results of in situ CO-DRIFTS), from which an approximative linear relationship is present (Fig. 3i). Furthermore, a positive correlation between intrinsic TOF and surface Ce^{3+} ratio (Supplementary Fig. 24) or surface oxygen vacancy ratio (Supplementary Fig. 25) is also demonstrated. The results above elucidate that the $Ir^{\delta+}$–O_v–Ce^{3+} interfacial sites serve as the intrinsic active center towards DRM reaction, accounting for the prominent catalytic performance.

Catalytic mechanism. In situ/*operando* XANES of Ir L_3-edge and Ce L_3-edge combined with *quasi* in situ XPS were applied to reveal the

https://doi.org/10.1038/s41467-024-48122-6

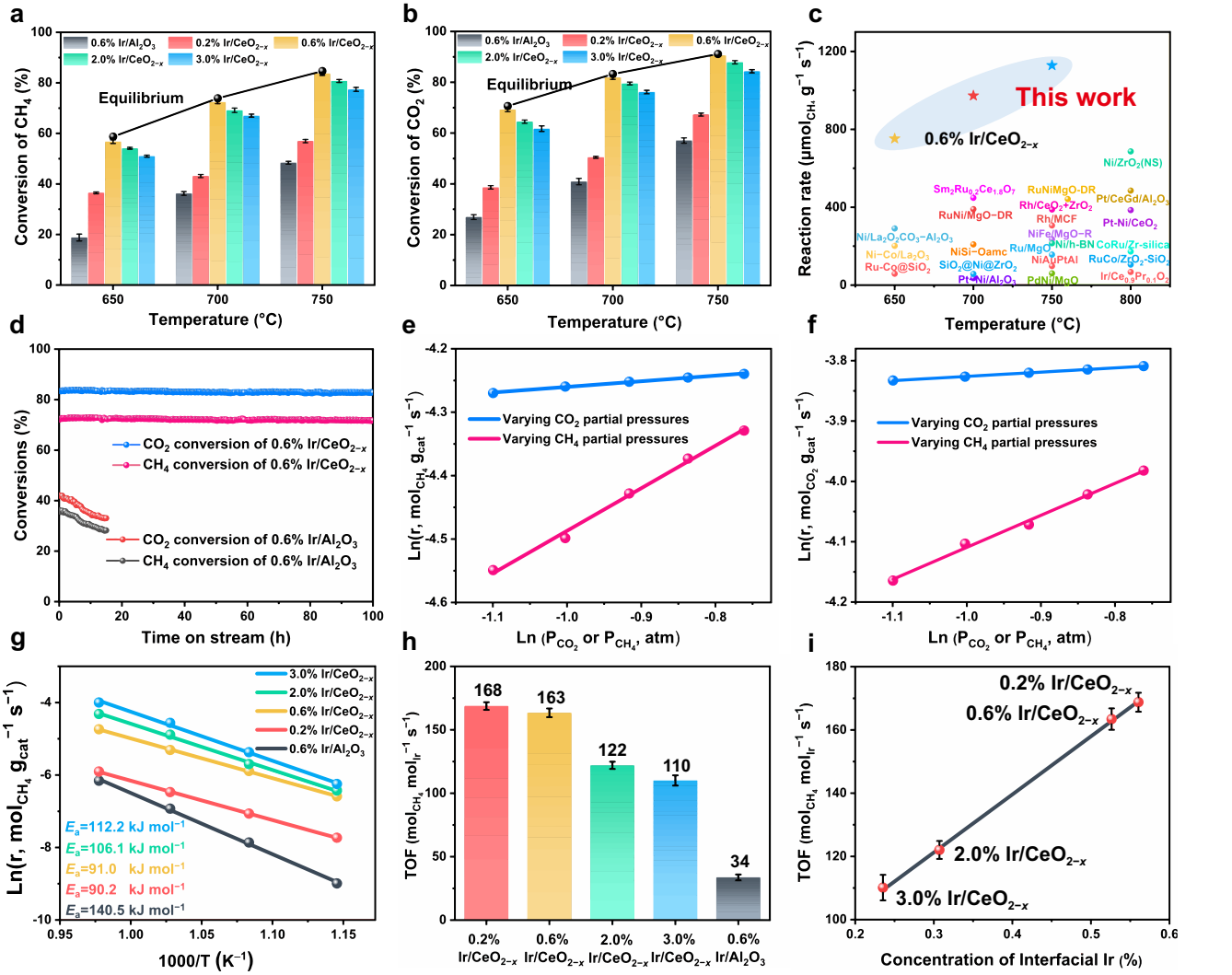

Fig. 3 | Catalytic performance of various catalysts. a, **b** CH_4 conversion and CO_2 conversion over various samples at 650, 700, and 750 °C. **c** Comparison study on mass specific activity between 0.6% Ir/CeO_{2-x} and other typical catalysts used in DRM reaction[64–79]. **d** Stability test of 0.6% Ir/CeO_{2-x} and 0.6% Ir/Al_2O_3 at 700 °C for DRM. Evaluated conditions: $CH_4/CO_2/N_2$ = 20/20/5 mL min^{-1}, GHSV = 240000 mL g^{-1} h^{-1}. **e**, **f** Correlation of CH_4 or CO_2 partial pressure on the reaction rates of CH_4 and CO_2. **g** Kinetic studies and calculated activation energy (E_a) of CH_4 over various catalysts. **h** Intrinsic TOF over various catalysts within the catalytic dynamic range. **i** TOF as a function of interfacial Ir concentration calculated by CO-DRIFTS results.

dynamic variation of fine structure and electronic interaction at interfacial sites under the catalytic reaction. During the measurement, CH_4 and CO_2 was introduced into the reaction cell in turn, and the catalytic reaction was triggered at 700 °C via injecting the second reactant gas, so as to observe the formation and variation of interface structure ($Ir^{\delta+}$–O_v–Ce^{3+}). When CH_4 is introduced alone, the white line peaks of Ir and Ce shift close to the reference Ir foil and CeF_3 (Fig. 4a, d), respectively, indicating a decline in valence states of Ir and Ce (Fig. 4b, e). The corresponding variations in XPS spectra of Ir 4*f* and Ce 3*d* are also observed (Fig. 4c, f): the $Ir^{\delta+}/(Ir^{\delta+}+Ir^0)$ ratio decreases whilst the $Ce^{3+}/(Ce^{3+} + Ce^{4+})$ ratio and O_v increase. This implies the occurrence of CH_4 dissociation to CH_x^* species, which then combines with surface reactive O to generate more $Ir^{\delta+}$–O_v–Ce^{3+} interface sites. After the injection of CO_2, the white line peaks of Ir and Ce shift back to their original position, indicating the replenishment of O_v by CO_2. In Fig. 4a, d, as CO_2 is introduced alone, the white line peaks of Ir and Ce move close to the reference IrO_2 and CeO_2, respectively (elimination of primary O_v); and XPS results show the increased valence states of Ir and Ce accompanied with reduced $Ce^{3+}/(Ce^{3+} + Ce^{4+})$ ratio and O_v (Fig. 4b, e). Afterwards, the subsequent CH_4 flowing induces the recovery of Ir and Ce white line peaks to their original position, corresponding to the CH_4 dissociation assisted with surface reactive oxygen species.

In situ/*operando* DRIFTS experiments of reactants were carried out to further identify the intermediate species and monitor the evolution of dynamic reaction process at the interface structure $Ir^{\delta+}$–O_v–Ce^{3+} (Fig. 5a–h). When CH_4 is introduced individually into the reactor at 700 °C, in addition to the gas phase CH_4 at ~3016 and ~1304 cm^{-1}, another two bands at ~1330 and ~1350 cm^{-1} corresponding to the deformation vibration of CH_x* and CH_3* are observed[4,20,51], respectively, due to the activation adsorption and dissociation of CH_4 at interface $Ir^{\delta+}$ sites. Subsequently, with the injection of CO_2, two strong peaks located at ~2360 and ~1550 cm^{-1}, as well as another broad one at ~3750–3550 cm^{-1} appear, which are attributed to the gas phase CO_2, the monodentate carbonate species (HCOO*) and surface hydroxyl group (OH*), respectively (Fig. 5b–d and Supplementary Figs. 28, 29)[16,20,54,55]. Notably, another IR band assigned to the CH_xO* species is found at ~1390 cm^{-1}, accompanied with the weakened bands of CH_4 and CH_x* species[56,57]. This is probably due to the oxidation of CH_x* by reactive oxygen species originating from CO_2 dissociation. In addition, three bands between ~2200 and ~2000 cm^{-1} are detected, which are ascribed to gaseous CO and adsorbed CO* at

https://doi.org/10.1038/s41467-024-48122-6

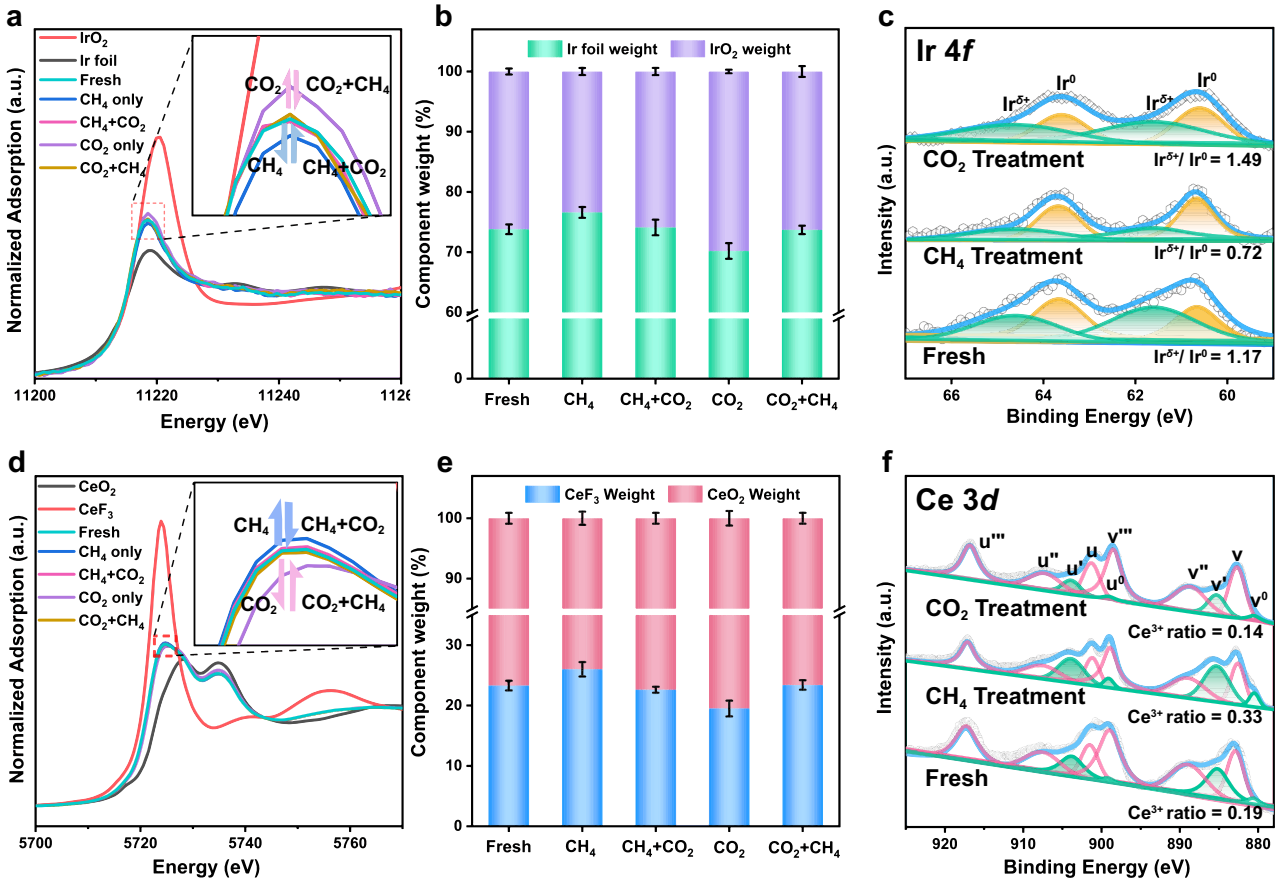

Fig. 4 | Local coordination structure and surface structure of 0.6% Ir/CeO_2 during DRM reaction. a, **b** In situ/*operando* normalized XANES at Ir L_3-edge and diagram of the linear combination fitting (LCF) results of 0.6% Ir/CeO_{2-x} with CH_4, CO_2 and $CH_4 + CO_2$ treatment, respectively. **d**, **e** Ce L_3-edge and diagram of the linear combination fitting (LCF) results of 0.6% Ir/CeO_{2-x} with CH_4, CO_2 and $CH_4 + CO_2$ treatment, respectively. **c**, **f** *Quasi* in situ XPS spectra of Ir 4*f* and Ce 3*d* for the fresh 0.6% Ir/CeO_{2-x} and the same catalyst after CH_4 or CO_2 treatment at 700 °C.

$Ir^{\delta+}$, respectively (Fig. 5c)[44–46]. Once the atmosphere is switched from the mixture gas (CO_2 and CH_4) to individual CH_4, the bands of gas phase CO_2 weaken firstly, and then the bands assigned to CH_xO^*, HCOO*, OH* and CO species disappear gradually accompanied with the enhancement of CH_4 and CH_x^* peaks. This demonstrates the oxygen-containing species (CH_xO^*, HCOO*, OH*) serves as important intermediate, whose consumption can be reproduced by CO_2 at interface O_v.

Next, we changed the study paradigm, in which CO_2 is injected into the reactor firstly under the same conditions. Accordingly, the bands assigned to CO_2 is observed (Supplementary Fig. 30 and Fig. 5e). With the subsequent flowing of CH_4, the bands of CH_4, CH_x^* and CH_3^* species are found (Fig. 5g, h), followed by the emergence of CH_xO^* and CO peaks as well as the weakened OH* band. This verifies the significance of CH_xO^* species originating from the reaction between CH_x^* and surface oxygen species, in accordance with the results of Fig. 5a–d. *Operando* investigations above (XAFS and DRIFTS) substantiate that the interface structure ($Ir^{\delta+}$–O_v–Ce^{3+}) serves as the intrinsic active center with a crucial synergistic effect: $Ir^{\delta+}$ promotes the activation adsorption of CH_4 molecule whilst CO_2 dissociation occurs at the Ce^{3+}–O_v site, followed by the formation of the key intermediate (CH_xO^* species).

To in-depth explore the decisive role of $Ir^{\delta+}$–O_v–Ce^{3+} interfacial sites in the reaction process, DFT calculations were investigated on Ir_1/CeO_{2-x} model based on the experimental results (Supplementary Fig. 31). As shown in Fig. 5i and Supplementary Fig. 32, firstly, CH_4 molecule undergoes adsorption at the interfacial $Ir^{\delta+}$ of Ir_1/CeO_{2-x} (110) with a small adsorption energy (−0.03 eV); then, the C–H bond cleavage of CH_4 occurs to generate CH_3^* (TS1: 1.12 eV). Afterwards, the CH_3^* species experiences dehydrogenation process which shows an energy barrier of 1.43 eV, excluding the oxidation of CH_3^* to CH_3O^* with a large steric hindrance. Subsequently, two possible steps are involved: (1) CH_2^* oxidation to CH_2O^* and (2) CH_2^* dehydrogenation to CH*. However, the former displays a much lower energy barrier (TS3: 1.03 eV) than the latter (TS4: 1.56 eV), in agreement with the formation of CH_xO^* intermediate verified by the *operando* DRIFTS results. This step is crucial, which inhibits excessive decomposition of CH_2^* species to carbon deposition. The next dehydrogenation of CH_2O^* to CHO* (TS5) and CO (TS6) shows normal activation barriers of 0.63 and 0.73 eV, respectively. Finally, the produced CO undergoes desorption from the O_v and the remaining four active hydrogen form into two H_2 molecules (Supplementary Fig. 32). Meanwhile, CO_2 molecule experiences dissociation adsorption at the O_v on the surface with an adsorption energy of −1.85 eV and an energy barrier of 0.7 eV (Supplementary Fig. 33 and 34), with the formation of active oxygen species that participates in the CH_2^* oxidation to CH_2O^*. According to the calculation results, the dehydrogenation of CH_3^* species to CH_2^* gives the highest energy barrier (1.43 eV), which is determined as the rate-determining step of DRM reaction, in accordance with the experimental results (Fig. 3e–f). In addition, a comparative study between Ir_1/CeO_{2-x} and Ir_1/Al_2O_3 shows that the reaction energy barrier of rate-determiningstep in the former case (1.43 eV) is significantly lower than the latter one (Supplementary Figs. 35, 36: 2.88 eV), demonstrating the essential contributions of interface sites ($Ir^{\delta+}$–O_v–Ce^{3+}), in well agreement with the catalytic performance in Fig. 3a–h.

In summary, we report an Ir/CeO_{2-x} catalytic system with metal–support interface structure towards DRM reaction. The

https://doi.org/10.1038/s41467-024-48122-6

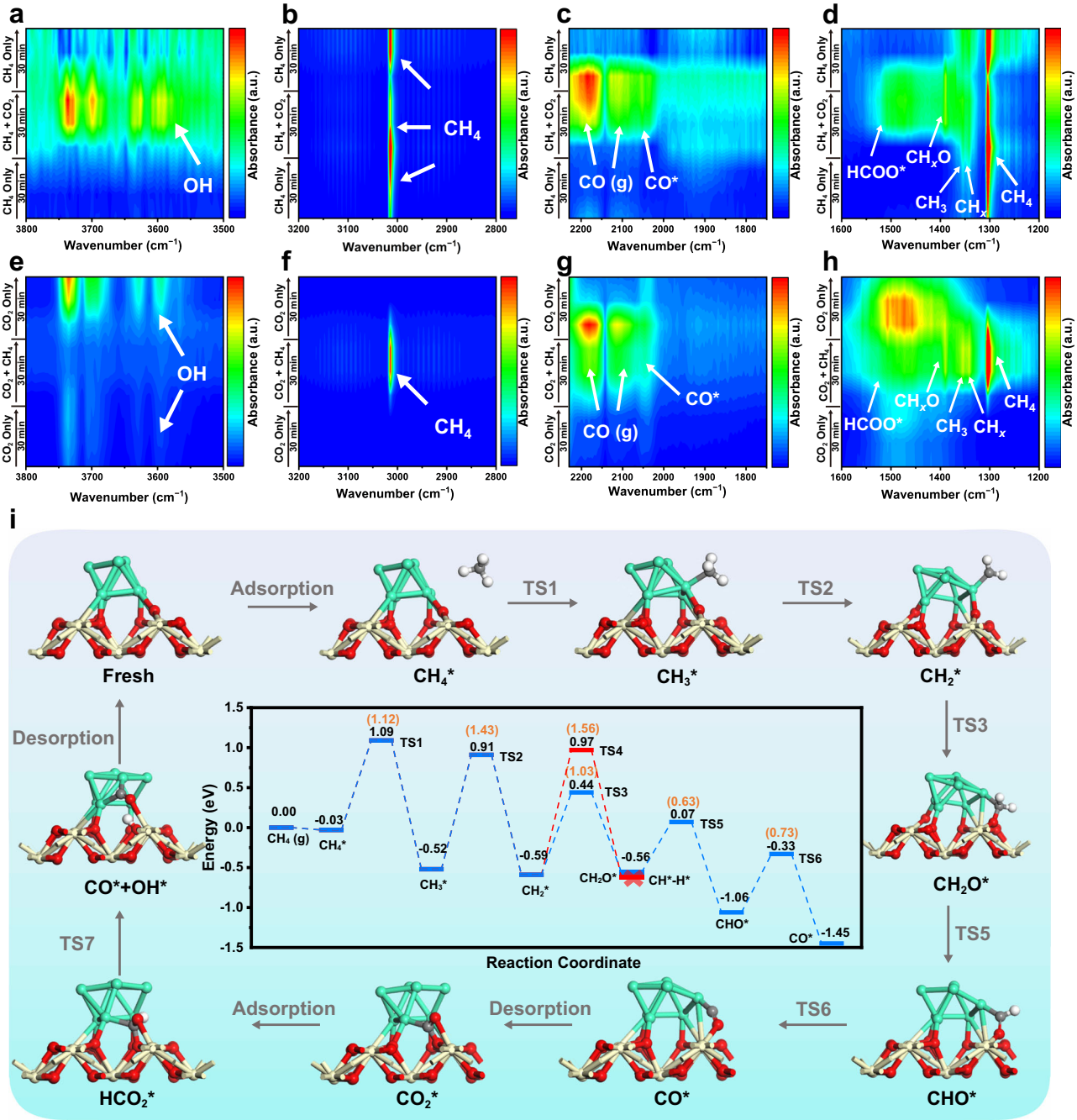

Fig. 5 | In situ/*operando* DRIFTS spectra and DFT calculations of DRM reaction on 0.6% Ir/CeO_{2-x}. In situ/*operando* DRIFTS spectra over 0.6% Ir/CeO_{2-x} at 700 °C after in-situ pretreatment and He purging, followed by exposure to: (**a**–**d**) first CH_4 atmosphere, subsequent $CH_4 + CO_2$ and then CH_4 atmosphere for 30 min, respectively; (**e**–**h**) first CO_2 atmosphere, subsequent $CO_2 + CH_4$ and then CO_2 atmosphere for 30 min, respectively. **i** Schematic illustration for DRM reaction at the interface of Ir/CeO_{2-x}. Ir, green; Ce, yellow; C, gray; O, crimson; H, white. The inset shows potential energy profile of CH_4 decomposition by Ir/CeO_{2-x}(110). 'TS' represents a transition state. The black and orange numbers represent the adsorption energies and energy barriers of the elementary steps, respectively.

obtained 0.6% Ir/CeO_{2-x} catalyst exhibits exceptional conversions of CH_4 (72%) and CO_2 (82%), a CH_4 reaction rate of ~973 $\mu mol_{CH4}\ g_{cat}^{-1}\ s^{-1}$ and a satisfactory service stability within 100 h at a relatively low temperature (700 °C). A joint investigation based on HAADF-STEM, *quasi* in situ XPS and in situ XAFS confirms the formation of interface structure ($Ir^{\delta+}$–O_v–Ce^{3+}), whose concentration can be modulated via adjusting the Ir loading. *Operando* investigations (DRIFTS and XAFS), catalytic evaluations and DFT calculations substantiate that the interfacial sites ($Ir^{\delta+}$–O_v–Ce^{3+}) serve as the intrinsic active center to facilitate the dissociation of CH_4 (the rate-determining step) and the oxidation of CH_2* to CH_2O*; the concomitant O_v can be replenished by the activation adsorption of CO_2. This interfacial synergistic catalysis plays a crucial role in boosting the catalytic performance and inhibiting deactivation, which paves a way for the design of other high-performance heterogeneous catalysts towards structure-sensitive reactions.

Methods

Chemicals and materials

Analytical grade chemical reagents were purchased in Aladdin company and used directly without further purification, including: $Ce(NO_3)_3{\cdot}6H_2O$, NaOH, Al_2O_3, and $H_2IrCl_6{\cdot}6H_2O$. Deionized water was adopted in all experiment steps.

Preparation of catalysts

CeO_2 nanorods were prepared via a hydrothermal method reported by our group[42]. Typically, $Ce(NO_3)_3$ solution (0.4 M, 20 mL) and NaOH solution (6.8 M, 140 mL) were fully mixed with vigorous stirring for 30 min at room temperature. The obtained milky slurry was placed into a 200 mL sealed Teflon autoclave for 24 h at 100 °C. After filtering, washing thoroughly, and drying at 65 °C for 18 h, the sample was calcined in air at 500 °C with a heating rate of 10 °C min^{-1} for 4 h to obtain the CeO_2 nanorods support. CeO_2 (0.5 g) was dispersed into deionized water (20 ml) and $H_2IrCl_6{\cdot}6H_2O$ aqueous solution (0.022 g mL^{-1}; 0.105, 0.315, 1.050, 1.575 mL, respectively) was slowly dripped into above solution with vigorous stirring for various Ir loading samples. After 8 h of reaction, the resulting precipitate was centrifuged, washed thoroughly with deionized water and ethanol, followed by drying at 60 °C for 12 h. Before the DRM reaction, the sample was pre-treated at 750 °C for 3 h in a gaseous mixture of CH_4 and CO_2 (1:1, v/v; total flow rate: 50 mL min^{-1}). As a reference, the Ir/Al_2O_3 sample was prepared via the same method described above by using Al_2O_3 as the support, in which the pre-treated steps are in accordance with those of Ir/CeO_{2-x} samples.

Characterizations

X-ray diffraction (XRD) experiments were carried out with Bruker D8 Advance diffractometer. The elemental content was determined by Shimadzu ICPS-7500 equipment. The morphology and structure of catalysts were studied on JEOL JEM-2010 high-resolution transmission electron microscope. AC-HAADF-STEM images and EDS mapping data were performed on JEOL JEM-ARM200F. The CO pulses chemisorption experiments were conducted on Micromeritics Autochem II 2920. *Quasi* in situ XPS measurements were recorded on Kratos Axis Ultra DLD Instrument. The pre-treated sample was placed in a glove box and transferred into a sample rod in a N_2 atmosphere. In situ/*Operando* XAFS at Ir L_3-edge and Ce L_3-edge measurements were recorded at the beamline BL11B of the Shanghai Synchrotron Radiation Facility (SSRF), Shanghai Institute of Applied Physics, Chinese Academy of Sciences (CAS). In situ/*operando* DRIFTS were studied on a Bruker TENSOR II infrared spectrometer with a MCT detector. The detailed experimental methods are present in the Supplementary Information.

DFT calculations

The density functional theory (DFT) calculations based on first-principle methodology were investigated using the Vienna ab initio simulation package (VASP 5.4.4)[58,59]. Generalized gradient approximation (GGA) of PBE functional was applied to describe the exchange and correlation energy. Grimme's DFT-D3 method and projector augmented wave (PAW) method were employed to illustrate the effect of van der Waals interaction and to depict the core electrons, respectively[60,61]. The climbing image nudged elastic band (CI-NEB) method was employed to determine reaction transition states[62,63].

Data availability

The primary data that support the plots within this paper and other finding of this study are available from the corresponding author on reasonable request. Source data are provided with this paper.

References

1. Zhao, H. et al. The role of Cu_1–O_3 species in single-atom Cu/ZrO_2 catalyst for CO_2 hydrogenation. *Nat. Catal.* **5**, 818–831 (2022).
2. Zito, A. M. et al. Electrochemical carbon dioxide capture and concentration. *Chem. Rev.* **123**, 8069–8098 (2023).
3. Song, Y. et al. Dry reforming of methane by stable Ni–Mo nanocatalysts on single-crystalline MgO. *Science* **367**, 777–781 (2020).
4. Xiao, Y. et al. Active exsolved metal-oxide interfaces in porous single-crystalline ceria monoliths for efficient and durable CH_4/CO_2 reforming. *Angew. Chem. Int. Ed.* **61**, e202113079 (2021).
5. Pakhare, D. et al. A review of dry (CO_2) reforming of methane over noble metal catalysts. *Chem. Soc. Rev.* **43**, 7813–7837 (2014).
6. Akri, M. et al. Atomically dispersed nickel as coke-resistant active sites for methane dry reforming. *Nat. Commun.* **10**, 5181 (2019).
7. Guo, D. et al. Enhanced thermocatalytic stability by coupling nickel step sites with nitrogen heteroatoms for dry reforming of methane. *ACS Catal.* **12**, 316–330 (2021).
8. Zhu, Q. et al. Enhanced CO_2 utilization in dry reforming of methane achieved through nickel-mediated hydrogen spillover in zeolite crystals. *Nat. Catal.* **5**, 1030–1037 (2022).
9. Tang, Y. et al. Synergy of single-atom Ni_1 and Ru_1 sites on CeO_2 for dry reforming of CH_4. *J. Am. Chem. Soc.* **141**, 7283–7293 (2019).
10. Zhang, X. et al. A novel Ni–MoC_xO_y interfacial catalyst for syngas production via the chemical looping dry reforming of methane. *Chem* **9**, 102–116 (2023).
11. Joo, S. et al. Enhancing thermocatalytic activities by upshifting the d-band center of exsolved Co–Ni–Fe ternary alloy nanoparticles for the dry reforming of methane. *Angew. Chem. Int. Ed.* **60**, 15912–15919 (2021).
12. Schwach, P. et al. Direct conversion of methane to value-added chemicals over heterogeneous catalysts: challenges and prospects. *Chem. Rev.* **117**, 8497–8520 (2017).
13. Meng, X. et al. Direct methane conversion under mild condition by thermo-, electro-, or photocatalysis. *Chem* **5**, 2296–2325 (2019).
14. Fan, L. et al. Strategies in catalysts and electrolyzer design for electrochemical CO_2 reduction toward C_{2+} products. *Sci. Adv.* **6**, eaay3111 (2020).
15. Li, X. et al. Selective visible-light-driven photocatalytic CO_2 reduction to CH_4 mediated by atomically thin $CuIn_5S_8$ layers. *Nat. Energy* **4**, 690–699 (2019).
16. Cheng, F. et al. Dry reforming of CH_4/CO_2 by stable Ni nanocrystals on porous single-crystalline MgO monoliths at reduced temperature. *Angew. Chem. Int. Ed.* **60**, 18792–18799 (2021).
17. Zhang, J.-C. et al. Robust ruthenium-saving catalyst for high-temperature carbon dioxide reforming of methane. *ACS Catal.* **10**, 783–791 (2019).
18. Zhang, X. et al. High-performance binary Mo–Ni catalysts for efficient carbon removal during carbon dioxide reforming of methane. *ACS Catal.* **11**, 12087–12095 (2021).
19. Niu, J. et al. Unraveling enhanced activity, selectivity, and coke resistance of Pt–Ni bimetallic clusters in dry reforming. *ACS Catal.* **11**, 2398–2411 (2021).
20. Liu, Z. et al. Highly active ceria-supported Ru catalyst for the dry reforming of methane: in situ identification of $Ru^{\delta+}$–Ce^{3+} interactions for enhanced conversion. *ACS Catal.* **9**, 3349–3359 (2019).
21. Danielis, M. et al. Outstanding methane oxidation performance of palladium-embedded ceria catalysts prepared by a one-step dry ball-milling method. *Angew. Chem. Int. Ed.* **57**, 10212–10216 (2018).
22. Köpfle, N. et al. Zirconium-assisted activation of palladium to boost syngas production by methane dry reforming. *Angew. Chem. Int. Ed.* **57**, 14613–14618 (2018).
23. Tavasoli, A. et al. Enhanced hybrid photocatalytic dry reforming using a phosphated Ni–CeO_2 nanorod heterostructure. *Nat. Commun.* **14**, 1435 (2023).
24. Palmer, C. et al. Dry reforming of methane catalysed by molten metal alloys. *Nat. Catal.* **3**, 83–89 (2020).
25. Kim, S. M. et al. Cooperativity and dynamics increase the performance of NiFe dry reforming catalysts. *J. Am. Chem. Soc.* **139**, 1937–1949 (2017).
26. Wu, Z. et al. Lattice srained Ni-Co alloy as a high-performance catalyst for catalytic dry reforming of methane. *ACS Catal.* **9**, 2693–2700 (2019).
27. Wei, J. et al. Structural and mechanistic requirements for methane activation and chemical conversion on supported iridium clusters. *Angew. Chem. Int. Ed.* **116**, 3771–3774 (2004).

28. Li, S. et al. Tuning the selectivity of catalytic carbon dioxide hydrogenation over iridium/cerium oxide catalysts with a strong metal-support interaction. *Angew. Chem. Int. Ed.* **56**, 10761–10765 (2017).
29. Li, H. et al. Synergetic interaction between neighbouring platinum monomers in CO_2 hydrogenation. *Nat. Nanotechnol.* **13**, 411–417 (2018).
30. Xu, M. et al. Insights into interfacial synergistic catalysis over Ni@TiO_{2-x} catalyst toward water–gas shift reaction. *J. Am. Chem. Soc.* **140**, 11241–11251 (2018).
31. Pu, T. et al. Engineering heterogeneous catalysis with strong metal–support interactions: characterization, theory and manipulation. *Angew. Chem. Int. Ed.* **62**, e202212278 (2022).
32. Chen, A. et al. Structure of the catalytically active copper–ceria interfacial perimeter. *Nat. Catal.* **2**, 334–341 (2019).
33. Parastaev, A. et al. Breaking structure sensitivity in CO_2 hydrogenation by tuning metal–oxide interfaces in supported cobalt nanoparticles. *Nat. Catal.* **5**, 1051–1060 (2022).
34. Meng, H. et al. A strong bimetal-support interaction in ethanol steam reforming. *Nat. Commun.* **14**, 3189 (2023).
35. Lustemberg, P. G. et al. Room-temperature activation of methane and dry re-forming with CO_2 on Ni-CeO_2(111) surfaces: effect of Ce^{3+} sites and metal–support interactions on C–H bond cleavage. *ACS Catal.* **6**, 8184–8191 (2016).
36. Maurer, F. et al. Tracking the formation, fate and consequence for catalytic activity of Pt single sites on CeO_2. *Nat. Catal.* **3**, 824–833 (2020).
37. Parastaev, A. et al. Boosting CO_2 hydrogenation via size-dependent metal–support interactions in cobalt/ceria-based catalysts. *Nat. Catal.* **3**, 526–533 (2020).
38. Pinheiro Araújo, T. et al. Flame-made ternary Pd–In_2O_3–ZrO_2 catalyst with enhanced oxygen vacancy generation for CO_2 hydrogenation to methanol. *Nat. Commun.* **13**, 5610 (2022).
39. Wang, F. et al. Active site dependent reaction mechanism over Ru/CeO_2 catalyst toward CO_2 methanation. *J. Am. Chem. Soc.* **138**, 6298–6305 (2016).
40. Wu, C. Y. et al. Inverse ZrO_2/Cu as a highly efficient methanol synthesis catalyst from CO_2 hydrogenation. *Nat. Commun.* **11**, 5767 (2020).
41. Jiang, F. et al. Insights into the influence of CeO_2 crystal facet on CO_2 hydrogenation to methanol over Pd/CeO_2 catalysts. *ACS Catal.* **10**, 11493–11509 (2020).
42. Wang, F. et al. Catalytic behavior of supported Ru nanoparticles on the {100}, {110}, and {111} facet of CeO_2. *J. Catal.* **329**, 177–186 (2015).
43. Meng, H. et al. Highly efficient hydrogen production from dehydrogenation reaction of nitrogen heterocycles via Pd^0–$Pd^{\delta+}$ synergistic catalysis. *ACS Catal.* **13**, 9234–9244 (2023).
44. Zhang, Y. et al. Tuning selectivity of CO_2 hydrogenation by modulating the strong metal–support interaction over Ir/TiO_2 catalysts. *Green. Chem.* **22**, 6855–6861 (2020).
45. Jin, R. et al. Low temperature oxidation of ethane to oxygenates by oxygen over iridium-cluster catalysts. *J. Am. Chem. Soc.* **141**, 18921–18925 (2019).
46. Ye, X. et al. Highly selective hydrogenation of CO_2 to ethanol via designed bifunctional Ir_1–In_2O_3 single-atom catalyst. *J. Am. Chem. Soc.* **142**, 19001–19005 (2020).
47. Lu, Y. et al. A versatile approach for quantification of surface site fractions using reaction kinetics: The case of CO oxidation on supported Ir single atoms and nanoparticles. *J. Catal.* **378**, 121–130 (2019).
48. Li, J. et al. Distribution and valence state of Ru species on CeO_2 supports: support shape effect and its influence on CO oxidation. *ACS Catal.* **9**, 11088–11103 (2019).
49. Safavinia, B. et al. Enhancing $Ce_xZr_{1-x}O_2$ activity for methane dry reforming using subsurface Ni dopants. *ACS Catal.* **10**, 4070–4079 (2020).
50. Wang, J. et al. Design of a carbon-resistant Ni@S–2 reforming catalyst: controllable Ni nanoparticles sandwiched in a peasecod-like structure. *Appl. Catal. B: Environ.* **282**, 119546 (2021).
51. Kim, S. et al. Yolk–shell Pt-NiCe@SiO_2 single-atom-alloy catalysts for low-temperature dry reforming of methane. *ACS Catal.* **11**, 8247–8260 (2021).
52. Yan, X. et al. Highly efficient and stable Ni/CeO_2–SiO_2 catalyst for dry reforming of methane: effect of interfacial structure of Ni/CeO_2 on SiO_2. *Appl. Catal. B: Environ.* **246**, 221–231 (2019).
53. Li, H. et al. Ultra-durable Ni-Ir/$MgAl_2O_4$ catalysts for dry reforming of methane enabled by dynamic balance between carbon deposition and elimination. *Chem. Catal.* **2**, 1748–1763 (2022).
54. Das, S. et al. Effect of partial Fe substitution in $La_{0.9}Sr_{0.1}NiO_3$ perovskite-derived catalysts on the reaction mechanism of methane dry reforming. *ACS Catal.* **10**, 12466–12486 (2020).
55. Xie, Y. et al. Frustrated lewis pairs boosting low-temperature CO_2 methanation performance over Ni/CeO_2 nanocatalysts. *ACS Catal.* **12**, 10587–10602 (2022).
56. Bu, K. et al. Methane dry reforming over boron nitride interface-confined and LDHs-derived Ni catalysts. *Appl. Catal. B: Environ.* **252**, 86–97 (2019).
57. Shen, D. et al. Synergistic Pt–CeO_2 interface boosting low temperature dry reforming of methane. *Appl. Catal. B: Environ.* **318**, 121809 (2022).
58. Kresse, G. et al. Efficiency of ab-initio total energy calculations for metals and semiconductors using a plane-wave basis set. *Comput. Mater. Sci.* **6**, 15–50 (1996).
59. Kresse, G. et al. Efficient iterative schemes forab initiototal-energy calculations using a plane-wave basis set. *Phys. Rev. B: Condens. Matter Mater. Phys.* **54**, 11169–11186 (1996).
60. Kresse, G. et al. From ultrasoft pseudopotentials to the projector augmented-wave method. *Phys. Rev. B: Condens. Matter Mater. Phys.* **59**, 1758–1775 (1999).
61. Blöchl, P. E. Projector augmented-wave method. *Phys. Rev. B: Condens. Matter Mater. Phys.* **50**, 17953–17979 (1994).
62. Yang, J. et al. A DFT+U study of acetylene selective hydrogenation on oxygen defective anatase (101) and rutile (110) TiO_2 supported Pd_4 cluster. *J. Chem. Phys.* **136**, 104107 (2012).
63. Heyden, A. et al. Efficient methods for finding transition states in chemical reactions: Comparison of improved dimer method and partitioned rational function optimization method. *J. Chem. Phys.* **123**, 224101 (2005).
64. Tsoukalou, A. et al. Dry-reforming of methane over bimetallic Ni–M/La_2O_3 (M = Co, Fe): the effect of the rate of $La_2O_2CO_3$ formation and phase stability on the catalytic activity and stability. *J. Catal.* **343**, 208–214 (2016).
65. Li, K. et al. Dry reforming of methane over $La_2O_2CO_3$-modified Ni/Al_2O_3 catalysts with moderate metal support interaction. *Appl. Catal. B: Environ.* **264**, 118448 (2020).
66. García-Diéguez, M. et al. Characterization of alumina-supported Pt, Ni and PtNi alloy catalysts for the dry reforming of methane. *J. Catal.* **274**, 11–20 (2010).
67. Dou, J. et al. Sandwiched SiO_2@Ni@ZrO_2 as a coke resistant nanocatalyst for dry reforming of methane. *Appl. Catal. B: Environ.* **254**, 612–623 (2019).
68. Zhou, H. et al. A single source method to generate Ru–Ni–MgO catalysts for methane dry reforming and the kinetic effect of Ru on carbon deposition and gasification. *Appl. Catal. B: Environ.* **233**, 143–159 (2018).
69. Naeem, M. A. et al. Exsolution of metallic Ru nanoparticles from fefective, fluorite-type solid solutions $Sm_2Ru_xCe_{2-x}O_7$ to impart stability on dry reforming catalysts. *ACS Catal.* **10**, 1923–1937 (2019).
70. Wu, H. et al. Bi- and trimetallic Ni catalysts over Al_2O_3 and Al_2O_3–MO (M = Ce or Mg) oxides for methane dry reforming: Au and Pt additive effects. *Appl. Catal. B: Environ.* **156–157**, 350–361 (2014).

71. Li, D. et al. Carbon dioxide reforming of methane over Ru catalysts supported on Mg–Al oxides: a highly dispersed and stable Ru/Mg(Al)O catalyst. *Appl. Catal. B: Environ.* **200**, 566–577 (2017).
72. Dong, J. et al. Reaction-induced strong metal–support interactions between metals and inert boron nitride nanosheets. *J. Am. Chem. Soc.* **142**, 17167–17174 (2020).
73. Qian, L. et al. The promotion effect of hydrogen spillover on CH_4 reforming with CO_2 over Rh/MCF catalysts. *Appl. Catal. B: Environ.* **164**, 168–175 (2015).
74. Yentekakis, I. V. et al. Effect of support oxygen storage capacity on the catalytic performance of Rh nanoparticles for CO_2 reforming of methane. *Appl. Catal. B: Environ.* **243**, 490–501 (2019).
75. Wang, F. et al. Tuning the metal-support interaction in catalysts for highly efficient methane dry reforming reaction. *Appl. Catal. B: Environ.* **180**, 511–520 (2016).
76. Whang, H. S. et al. Enhanced activity and durability of Ru catalyst dispersed on zirconia for dry reforming of methane. *Catal. Today* **293–294**, 122–128 (2017).
77. Araiza, D. G. et al. Dry reforming of methane over Pt–Ni/CeO_2 catalysts: effect of the metal composition on the stability. *Catal. Today* **360**, 46–54 (2021).
78. da Fonseca, R. O. et al. Study of the effect of Gd-doping ceria on the performance of Pt/$GdCeO_2$/Al_2O_3 catalysts for the dry reforming of methane. *Catal. Today* **355**, 737–745 (2020).
79. Tathod, A. P. et al. Mediating interaction strength between nickel and zirconia using a mixed oxide nanosheets interlayer for methane dry reforming. *Appl. Catal. B: Environ.* **249**, 106–115 (2019).

Acknowledgements

This work was supported by the National Key R&D Program of China (2021YFC2103500), the National Natural Science Foundation of China (22172006, 22102006, 22288102, and 22109177), and the Young Elite Scientists Sponsorship Program by CAST (2023QNRC001). The authors are thankful for the support of the SSRF (Shanghai Synchrotron Radiation Facility) during the XAFS measurements at the beamline of BL11B.

Author contributions

M.W., Y.Y., G.C. and H.W. conceived the idea and designed the research. H.Y. and H.L. performed the DFT calculations. H.W., Z.L. and H.M. synthesized the catalysts and conducted the characterizations and reaction tests. L.W. and J.L. helped the STEM and XAFS analysis. All the authors analyzed the data and wrote the paper.

Competing interests

The authors declare no competing interests.

Additional information

Supplementary information The online version contains supplementary material available at https://doi.org/10.1038/s41467-024-48122-6.

Correspondence and requests for materials should be addressed to Guoqing Cui, Yusen Yang or Min Wei.

Peer review information *Nature Communications* thanks Petar Djinović and the other, anonymous, reviewers for their contribution to the peer review of this work. A peer review file is available.